Journal Name

ARTICLE TYPE

Cite this: DOI: 00.0000/xxxxxxxxxx

Understanding the asymmetry between advancing and receding microscopic contact angles

T. Omori,*[a] Y. Kobayashi,[a] Y. Yamaguchi[a] and T. Kajishima[a]

Received Date
Accepted Date

DOI: 00.0000/xxxxxxxxxx

By means of molecular dynamics simulation, the advancing and receding microscopic contact angles were analyzed for a shear flow of two mono-atomic fluids confined between parallel non-polar solid walls. We defined the microscopic dynamic contact angle based on the coarse-grained microscopic density distribution of the fluids (the instantaneous interface method [Willard and Chandler, J. Phys. Chem. B **114**, 1954–1958 (2010)]) near the moving contact line. We have found that the asymmetric change of fluid density near the wall with respect to the moving contact line results in a different dependence between the advancing and receding contact angles on the contact line velocity in a system where the two fluids across the interface have unequal wettability to the solid wall. This difference between the advancing and receding contact angles leads to different flow resistance caused by the advancing and receding contact lines, which should have impact on the industrial applications of the fine fluid transportation with contact lines.

1 Introduction

The prediction of dynamic wetting is of significant theoretical and practical interest, and measuring and modeling of dynamic contact angles (CAs) have been an active subject of research over the last decades[1,2]. One of the fundamental problems toward the modeling of dynamic CAs is the possible arbitrariness in its definition. They may be totally different depending on which part of the fluid interface is considered to form an angle to the solid surface. In particular, there is even a qualitative difference between the microscopic dynamic CA measured in the molecular vicinity of the contact line (CL) and the macroscopic dynamic CA measured elsewhere[3–5].

In terms of predicting the flow with CLs, it has been demonstrated[6] that the microscopic dynamic CA is a more fundamental quantity than the macroscopic dynamic CA and is a more suitable quantity to be implemented in the boundary condition for the fluid momentum equation (see also Qian *et al.*[7]). There have been attempts to measure or estimate the microscopic dynamic CA by molecular dynamics (MD) simulation[8–11], by dynamic density functional theory (DDFT)[12,13] or by a unique combination of precise experiments and theories[14]; however the dependence of the microscopic dynamic CA on the CL velocity, which is essential to develop the boundary condition for the fluid momentum equation with moving CLs, has been little[10,11] explored. Such boundary condition should have an essential importance particularly in hybrid MD/continuum approaches[15,16], which are now increasingly feasible.

It is believed that MD simulation is a promising tool to investigate the microscopic physics near moving CLs, but no clear definition of the dynamic CA has been made so far (in e.g.[8–10,17,18]) from the microscopic point of view: fitting the interface to a circular arc to measure CAs is only valid for a droplet under static conditions without gravity[19]. In fact, fitting a different portion of a droplet profile to a circular arc can result in a significant difference in the measured dynamic CA[20].

In the present study by means of MD simulation, the advancing and receding dynamic CAs (ACA and RCA, respectively) in the vicinity of the CL were obtained by measuring the tangents of the *instantaneous interfaces*[21,22] at a distance of a few adsorption layers (layers in fluid of high density) from the solid surface. A similar attempt has been made recently by Smith *et al.*[11] using a cluster-based interface capturing, but their focus was on the fluctuation in the CAs and much attention was not devoted to the difference between the advancing and receding CAs. An interface-capturing method, called the intrinsic sampling method[23], was also adopted to elucidate the mechanism of the thermal resistance across a fluid-fluid interface[24] and also to derive an Irving-Kirkwood like formula for the pressure tensor across a liquid-vapour interface that is valid for systems away from equilibrium[25]. As we see later, the present measurement procedure adopting the instantaneous interface method enabled us to extract the structures of the flow and the interface near the moving CLs, which were not smeared by the thermal fluctuations, and to discuss the difference between the advancing and receding CAs.

[a] *Department of Mechanical Engineering, Osaka University, 2-1 Yamadaoka, Suita, Osaka 565-0871, Japan. E-mail: t.omori@mech.eng.osaka-u.ac.jp*

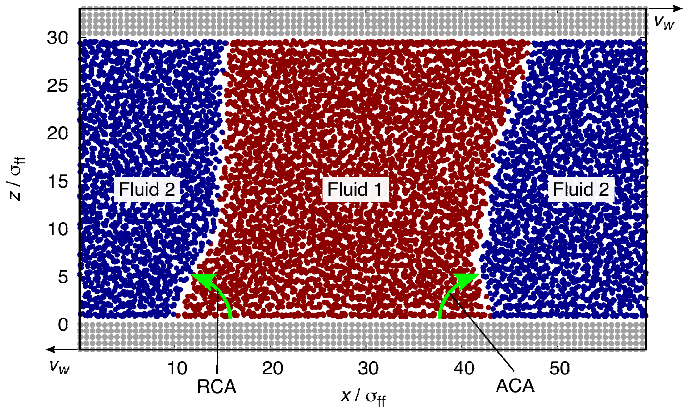

Fig. 1 Snapshot of the system, a shear flow of two immiscible liquids, where the equilibrium CA θ_e and the wall velocity v_w were 75° and $0.020\sqrt{\varepsilon_{ff}/m_f}$, respectively. The positions of the atoms and molecules are projected on a xz plane. The origin of the z axis was defined on the innermost (001) plane of the bottom FCC crystal. The length L_x, the width L_y and the height L_z of the channel were $59.4\sigma_{ff}$, $7.7\sigma_{ff}$ and about $30.5\sigma_{ff}$, respectively. The height L_z varied slightly (1%) under different simulation conditions due to the system pressure control. The temperature control (Langevin thermostat) was applied on the second outermost layers of the wall. The boundaries normal to the wall surface were all periodic.

Based on the unsmeared fluid density distribution near the CLs, we show that in the definition of the microscopic CA the first adsorption layer must be avoided. This is reminiscent of the observation by Bocquet and Barrat [26] and also by Chen *et al.* [27] in the definition of the hydrodynamic boundary to the solid wall for a single phase fluid. This correspondence has a potential importance in the development of a hydrodynamic boundary condition with moving CLs.

2 Problem formulation and methods for simulation

In the present study, two immiscible mono-atomic fluids were confined and sheared by two parallel non-polar solid walls moving at a constant velocity v_w in opposite directions: a snapshot of the system is shown in Fig. 1. We had 4900 molecules for each fluid and 5520 atoms for the walls. We measured all the CAs, the ACA, RCA and equilibrium CAs from the side of fluid 1. Similarly we call the CLs advancing or receding with respect to fluid 1. For the interaction potential between the fluid molecules and between the solid and fluid molecules, the 12-6 Lennard-Jones (LJ) potential was adopted:

$$\Phi_{LJ}(r_{ij}) = 4\varepsilon_{\alpha\beta}\left[\left(\sigma_{\alpha\beta}/r_{ij}\right)^{12} - \delta_{\alpha\beta}\left(\sigma_{\alpha\beta}/r_{ij}\right)^{6}\right], \qquad (1)$$

where r_{ij} is the distance between molecules i and j. We set the parameters (Tab. 1) so that we investigated the two cases with respect to the equilibrium CA θ_e, namely $\theta_e = 90$, 75°. In the present study, a quadratic function was added to the RHS of eqn (1) so that $\Phi_{LJ}(r_{ij})$ and $\Phi'_{LJ}(r_{ij})$ smoothly vanished at the cut-off distance $r_{ij} = 2.5\sigma_{\alpha\beta}$. The equations of motion were integrated by means of the velocity Verlet algorithm with a time step of $2.69\times10^{-3}\sqrt{m_f\sigma_{ff}^2/\varepsilon_{ff}}$. Each solid wall consisted of 5 layers of atoms in the (001) plane of a FCC crystal with a lattice constant of $0.91\sqrt{2}\sigma_{ff}$; therefore, the wall surface was atomistically smooth. The interaction between the wall atoms was described by the harmonic potential between the nearest neighbors

(α,β)		$\sigma_{\alpha\beta}$ [Å]	$\varepsilon_{\alpha\beta}$ [J]	$\delta_{\alpha\beta}$ [-]
(f_I, f_J)	if $I = J$	3.40	1.67×10^{21}	1
	if $I \neq J$	3.40	1.67×10^{21}	−1
(f_1, s)	if $\theta_e = 90°$	$1.04\,\sigma_{f_1f_1}$	$1.16\,\varepsilon_{f_1f_1}$	1
	if $\theta_e = 75°$	$1.04\,\sigma_{f_1f_1}$	$1.16\,\varepsilon_{f_1f_1}$	1
(f_2, s)	if $\theta_e = 90°$	$1.04\,\sigma_{f_2f_2}$	$1.16\,\varepsilon_{f_2f_2}$	1
	if $\theta_e = 75°$	$1.04\,\sigma_{f_2f_2}$	$0.928\,\varepsilon_{f_2f_2}$	1

Table 1 Parameters in the LJ potential. The letters "f" and "s" represent fluid and solid, respectively, and the subscripts to "f" take either 1 or 2 to denote the fluid type. These subscripts may be omitted in the case without ambiguity. Fluids of the two different types are immiscible to each other with $\delta = -1$ [7,18,28]. According to Thompson and Robbins [18], the CA behaviour is not affected by the value of δ when $-1 \le \delta \le 0$. The angle θ_e denotes the equilibrium CA measured from the side of fluid 1.

$$\Phi_H(r_{ij}) = k(r_{ij} - r_0)^2/2 \qquad (2)$$

with $k = 3.24\times10^3\varepsilon_{ff}/\sigma_{ff}^2$ and $r_0 = 0.91\sigma_{ff}$. The sheared flows were generated by moving the outermost layers of the solid walls at constant speeds and the temperature of the system was controlled at $1.10\varepsilon_{ff}/k_B$ by applying the Langevin thermostat [29] on the layers next to the shear generating layers. The thermostatting layer was placed far enough from the liquid so that the thermostatted wall atoms did not directly interact with the liquid molecules. We limited the temperature control to the atom velocities in the $x-y$ plane to avoid the fluctuation in the system pressure as a possible side-effect. The system temperature remained within $0.06\varepsilon_{ff}/k_B$ of the target temperature throughout the simulations. The magnitude of the velocity gradient observed in the present study was no more than $0.03\sqrt{\varepsilon_{ff}/m_f\sigma_{ff}^2}$, for which one expects [30] the flow to be in the linear response regime. The height of the channel was determined [31,32] so that the system pressure was $1.65\varepsilon_{ff}/\sigma_{ff}^3$: the two fluids were in the liquid state and there was no formation of vapor during the simulations.

The CA and the CL velocity were measured from a level set of the coarse-grained density field [22] defined as

$$\overline{\rho_I}(\boldsymbol{r}) = \sum_{i\in f_I}\phi(|\boldsymbol{r}-\boldsymbol{r}_i|) \qquad (3)$$

with

$$\phi(r) = \exp\left(-r^2/2\xi^2\right)/2\pi\xi^2, \qquad (4)$$

where $\boldsymbol{r}_i$ is the coordinate of fluid molecule i of type I ($I = 1,2$) in the xz plane considering the two-dimensionality of the present system. The instantaneous interface profile was obtained by finding $\boldsymbol{r}$ that satisfied $\overline{\rho_1}(\boldsymbol{r}) = \overline{\rho_2}(\boldsymbol{r})$. We employed $\xi = 0.28\sigma_{ff}$ to resolve the layer structure of the fluid (the so-called adsorption layers) formed near the walls. The position of the instantaneous CL was obtained as the intersection of the instantaneous interface profile and $z = 0$. The equilibrium position of the innermost layer of the bottom wall was defined as $z = 0$ (see Fig. 1). The instantaneous density and velocity distributions with its origin at the

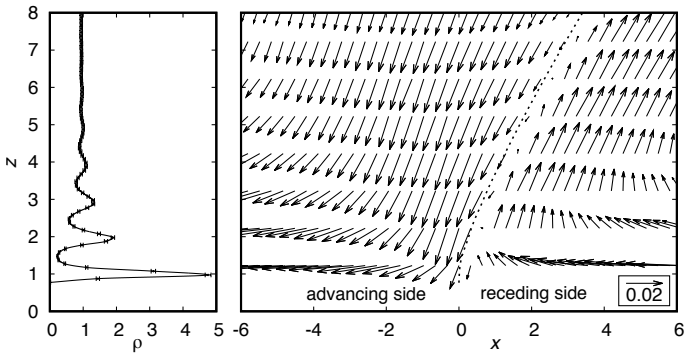

Fig. 2 (Left) Density distribution ρ of the fluid near the wall surface measured in a region away from the fluid-fluid interfaces ($\theta_e = 90°$). (Right) Velocity distribution near the CL formed on the bottom wall that was moving in the $-x$ direction ($\theta_e = 90°$). The dotted line denotes the interface profile.

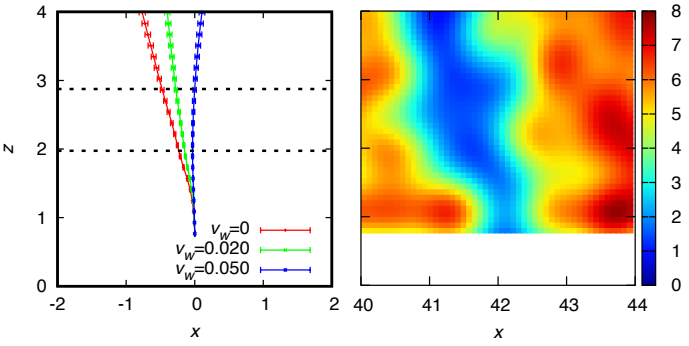

Fig. 3 (Left) Time-averaged interface profiles under different wall velocities v_w near the advancing CL ($\theta_e = 75°$). The bottom wall was moving in the $-x$ direction. The dotted lines denote the positions of the second and the third adsorption layers. (Right) Instantaneous coarse-grained density profile, $\overline{\rho_1} + \overline{\rho_2}$ (eqn 3), near the CL under $v_w = 0$ ($\theta_e = 75°$).

instantaneous CL were collected to calculate their time-averages.

To estimate the statistical uncertainty in time-averaged quantities, 200 independent simulations with different random number series in the Langevin thermostat were conducted. Each simulation was conducted for $3.77 \times 10^3 \sqrt{m_f \sigma_{ff}^2 / \varepsilon_{ff}}$ in time after the system was equilibrated and reached a steady state. In the following, all physical quantities are non-dimensionalized by m_f, σ_{ff} and ε_{ff} and these bases for the reduced units are not shown for the sake of brevity.

3 Results and discussions

3.1 Flow field and the definition of the microscopic CA

Figure 2 shows the time-averaged density and velocity distributions of the fluids near the moving wall for $\theta_e = 90°$. The left panel of the figure shows the density distribution of the fluids away from the fluid-fluid interfaces, where the existence of the adsorption layers were exhibited. The location of the adsorption layers was identical for $\theta_e = 90°$ and $75°$ because of the identical σ_{fs} in the present study. Shown in the right panel of the figure is the velocity distribution near the moving CL for $\theta_e = 90°$. The velocity distribution for $\theta_e = 75°$ was qualitatively the same. By virtue of the instantaneous interface method, a continuous velocity field, which had a corner-flow like structure, was extracted with a high spacial resolution. We can observe that there is a maximum slip velocity on the CL, which should regularize the stress singularity on the CL.

The left panel of Fig. 3 shows the time-averaged interface profiles near the advancing CL for $\theta_e = 75°$ under different wall velocities.The interface around $z = 1$ was perpendicular to the wall surface regardless of the wall velocity even if $\theta_e \neq 90°$. The right panel of Fig. 3 shows an instantaneous coarse-grained density distribution of the fluids, $\overline{\rho_1} + \overline{\rho_2}$ (eqn 3), near the same CL as in the left panel ($\theta_e = 75°$) under the static condition. As we can see from the figure, there was always an isolated density contour around the first adsorption layer ($z = 1$), where no meaningful interface profile regarding the CL dynamics can be extracted. We therefore calculated the microscopic CAs as the linear-interpolation of the interface profiles between the second and the third adsorption layers as the nearest possible measurement location from the solid wall; the equilibrium CAs were measured in the same way.

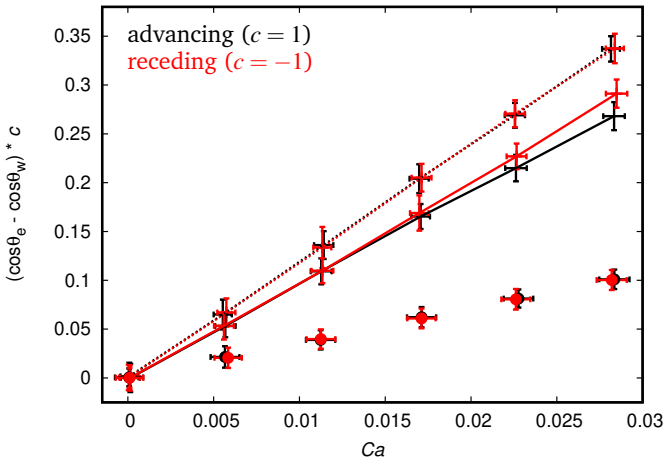

Fig. 4 Dependence of the advancing and receding microscopic dynamic CAs θ_w on the CL velocity v_{CL}. The CL velocity is shown as $Ca = \eta v_{CL}/\gamma$, where η is the fluid viscosity and γ is the interfacial tension between the two fluids. The error-bars are shown for both axes. The broken lines are for $\theta_e = 90°$ with $\varepsilon_{f_1 s} = \varepsilon_{f_2 s} = 1.16$ and solid lines for $\theta_e = 75°$ with $\varepsilon_{f_1 s} = 1.16$ and $\varepsilon_{f_2 s} = 0.928$. The symbols show the results for the system where the two solid-fluid interaction parameters were equally halved from $\varepsilon_{f_1 s} = \varepsilon_{f_2 s} = 1.16$ to $\varepsilon_{f_1 s} = \varepsilon_{f_2 s} = 0.58$ and thus θ_e remained $90°$.

3.2 Dynamics of the microscopic CA

Shown in Fig. 4 is the dependence of the microscopic CA on the CL velocity v_{CL} for two systems with different equilibrium CAs $\theta_e = 90°$ and $75°$ respectively, where the microscopic CA θ_w was shown in the form $\cos\theta_e - \cos\theta_w$, a non-dimensionalized uncompensated Young stress [1], as a function of the capillary number Ca defined as $\eta v_{CL}/\gamma$, where η is the fluid viscosity and γ is the interfacial tension between the two fluids. No hysteresis was observed on the atomistically smooth surface investigated in the present study. The figure indicates that the uncompensated Young stress has a linear dependence on the CL velocity regardless of θ_e as recently reported in the literature [10]. What deserves attention is

that a slight difference was observed between the ACA and the RCA for $\theta_e = 75^\circ$ while they were identical for $\theta_e = 90^\circ$.

There are a number of models that relate the dynamic CA to the CL velocity, such as the model by Kistler[33] based on the experimental data by Hoffman[34], the Hoffman-Voinov-Tanner law[33,35], the pure hydrodynamic models[36,37] and the molecular kinetic theory (MKT)[38] to mention a few. In principle, only the MKT describes the *microscopic* dynamic CA. The MKT formula written[39] as $\cos\theta_e - \cos\theta_w = \alpha\exp[\gamma(1+\cos\theta_e)/(k_BT)]Ca \propto Ca$, where γ is the fluid interfacial tension, T is the temperature, and α is a constant that depends on the fluid molecule size and the solid lattice constant, does not capture the observed difference between the ACA and the RCA. Note that this formula is describing one-fluid systems in the small Ca regime and it is fair to say that the theory is under development for two-fluid systems[8,20].

To investigate the reason for the different behaviours of dynamic CA under different equilibrium CAs observed in Fig. 4, we measured the density distribution of the fluids near the CL in the first adsorption layer. It should reveal the mechanical interaction between the solid wall and the fluids because the first adsorption layer is responsible for the friction between the solid wall and the fluids: the friction force is the summation of the tangential force between each solid atom and fluid molecule and it has been reported that this summation almost saturates to the total friction force in the first adsorption layer[7,40–42]. Figure 5 shows such distribution on the bottom wall near the advancing and receding CLs for two systems with different equilibrium CAs $\theta_e = 90^\circ$ and 75° respectively. The density on the advancing side decreased and the density on the receding side slightly increased in both systems by increasing the wall velocity. It was due to the corner flow where the pressure is decreased on the advancing side and increased on the receding side[6]. Note that we have observed the height of the first adsorption layer remained the same although its fluid density was affected by the flow.

The asymmetric change of fluid density in the first adsorption layer with respect to the CL resulted in the difference between the solid-fluid friction around the advancing and receding CLs when $\theta_e = 75^\circ$. For $\theta_e = 75^\circ$, the affinity of the wall to the fluid molecules on the two sides of the CL were different and the integrated friction around the CLs was larger for the receding CL than for the advancing CL (the CLs are called advancing or receding with respect to fluid 1 as we defined at the beginning of section 2). When $\theta_e = 90^\circ$, the fluid molecules on both sides of the CL had the identical affinity to the wall and therefore the asymmetric density change near the CL did not cause difference in the solid-fluid friction between the advancing and receding CLs.

How does the solid-fluid friction affect the dynamic CA? This is what we want to address now. At the solid-fluid boudary near the CL, the solid-fluid friction force on the solid side is equal to the summation of the capillary and the viscous forces on the fluid side. If we consider the capillary force is equal to the integration of the uncompensated Young stress across the CL[7], the mechanical balance at the solid-fluid boundary is written[6] as

$$\int_{\text{int}} \left(\frac{u_t^{*\text{slip}}}{l^*} - \frac{\partial u_t^*}{\partial x_n^*} \right) dx_t^* = \frac{v_{\text{CL}}^*}{Ca}(\cos\theta_e - \cos\theta_w), \qquad (5)$$

where the subscripts t and n denote tangential and normal to the wall surface respectively and the asterisk denotes that the variables are non-dimensionalized. The shear rate of the flow on the boundary is written as $\partial u_t/\partial x_n$, v_{CL} is the CL velocity relative to the wall, u_t^{slip} is the fluid slip velocity and l is the slip length that is inversely proportional to the solid-fluid friction coefficient. The friction coefficient is the friction force per unit wall surface area divided by the fluid slip velocity and larger for the solid-fluid pair with stronger affinity. Because the LHS of eqn (5) and the CL velocity v_{CL} on the RHS approximately scale with the slip velocity u_t^{slip} on the CL, there is a linear relationship $\cos\theta_e - \cos\theta_w \propto Ca$ as we have observed in Fig. 4. As the second term on the LHS of eqn (5) was one order of magnitude smaller than the first term on the LHS of eqn (5) in the systems investigated, we see that the proportionality constant $(\cos\theta_e - \cos\theta_w)/Ca$ mainly depended on the slip length near the CL and therefore, it was larger for the RCA than for the ACA under $\theta_e = 75^\circ$. The globally larger proportionality constant for $\theta_e = 90^\circ$ than for $\theta_e = 75^\circ$ can be similarly explained.

The importance of considering the solid-fluid friction in the prediction of the dynamic CA is further evident when we observe the results under different solid-fluid interaction parameters. Figure 4 also compares the behaviours of the microscopic dynamic CA under the halved solid-fluid interaction parameters ($\varepsilon_{\text{f1s}} = \varepsilon_{\text{f2s}} = 0.58$, shown with symbols) and under the original parameters ($\varepsilon_{\text{f1s}} = \varepsilon_{\text{f2s}} = 1.16$) for $\theta_e = 90^\circ$. This result illustrated that even under the same equilibrium CA the dynamic CAs were different when the solid-fluid friction coefficients were different.

Remarks should be made here about the assumption to derive eqn (5). In the derivation, it was assumed that the capillary force near the moving CL can be described by the uncompensated Young stress. This assumption, however, is probably not true. Considering the density change in the first adsorption layer induced by the flow that we have seen in Fig. 5, the equilibrium contribution in the capillary force may deviate[19] from $\cos\theta_e$. How this deviation can affect the seemingly linear relationship $\cos\theta_e - \cos\theta_w \propto Ca$ should be addressed in future works.

4 Concluding remarks

By means of molecular dynamics simulation, we have analyzed the advancing and receding microscopic contact angles formed by two immiscible mono-atomic fluids and a non-polar solid wall. In the definition of the microscopic contact angle, the first adsorption layer on the wall was excluded based on the high-resolution density profile of the fluids near the contact line obtained by the instantaneous interface method. The contact angle was measured by the local interface tangent without resorting to circular-arc fitting of the moving fluid-fluid interface.

We demonstrated that the uncompensated Young stress was proportional to the capillary number under the whole range of the capillary number up to 0.03. We have found the difference in the constant of proportionality between the advancing and receding contact angles when the equilibrium contact angle is not 90 degrees and this difference can be attributed to the asymmetric density change near the moving contact line induced by the corner flow. We hope that the present results provide useful in-

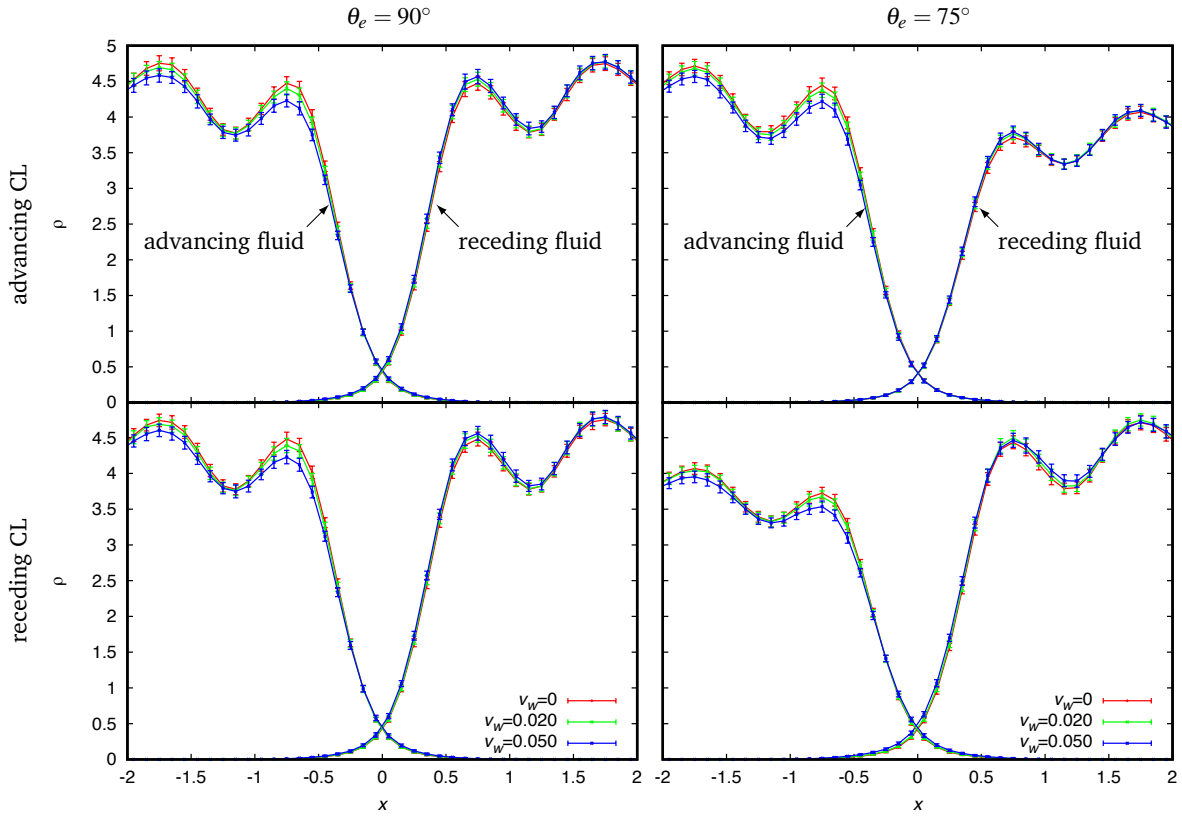

Fig. 5 Influence of the wall velocity on the density distribution of the two fluids in the first adsorption layer near the advancing and receding CLs. The CLs are called advancing or receding with respect to fluid 1 as we defined at the beginning of section 2. The corner flows near the CL caused asymmetric changes in the density distribution with respect to the CLs.

formation also to be integrated into the existing state-of-the-art dynamic contact angle models.

To conclude, we would like to address the practical aspect of the findings of the present study. Writing the advancing and receding contact angles as $\theta_{w,a}$ and $\theta_{w,r}$ respectively, the total capillary force imposed on the flow is $2\gamma(\cos\theta_{w,a} - \cos\theta_{w,r})$ per unit channel width if we neglect the possible variation of the equilibrium contribution due to the flow. The total capillary force can then be expressed as $2\gamma(\cos\theta_{w,a} - \cos\theta_{w,r}) = -2(\alpha_a + \alpha_r)Ca$, where the coefficients α_a and α_r are the slopes in Fig. 4 for the advancing and receding contact angles, respectively. It means that more resistance was induced around the receding contact line than around the advancing contact line in systems with $\theta_e < 90°$. This phenomenon should have impact on the industrial applications of the two-component or two-phase fluid transportation in fine pores.

Conflicts of interest

There are no conflicts to declare.

Acknowledgements

This work was financially supported by JSPS KAKENHI Grant Nos. 15K17974, 18K03929 and 18K03978. YY was also supported by JST CREST Grant No. JPMJCR18I1, Japan. The authors thank Laurent Joly of Université Lyon 1 for fruitful discussions.

References

1 D. Bonn, J. Eggers, J. Indekeu and J. Meunier, *Rev. Mod. Phys.*, 2009, **81**, 739–805.
2 J. H. Snoeijer and B. Andreotti, *Annu. Rev. Fluid Mech.*, 2013, **45**, 269–292.
3 N. G. Hadjiconstantinou, *Phys. Rev. E*, 1999, **59**, 2475–2478.
4 E. Ramé, S. Garoff and K. R. Willson, *Phys. Rev. E*, 2004, **70**, 031608.
5 J. H. Snoeijer, *Phys. Fluids*, 2006, **18**, 021701.
6 T. Omori and T. Kajishima, *Phys. Fluids*, 2017, **29**, 112107.
7 T. Qian, X.-P. Wang and P. Sheng, *Phys. Rev. E*, 2003, **68**, 016306.
8 D. Seveno, T. D. Blake, S. Goossens and J. De Coninck, *Langmuir*, 2011, **27**, 14958–14967.
9 A. Malani, A. Raghavanpillai, E. B. Wysong and G. C. Rutledge, *Phys. Rev. Lett.*, 2012, **109**, 184501.
10 T. D. Blake, J.-C. Fernandez-Toledano, G. Doyen and J. De Coninck, *Phys. Fluids*, 2015, **27**, 112101.
11 E. R. Smith, E. A. Müller, R. V. Craster and O. K. Matar, *Soft Matter*, 2016, **12**, 9604–9615.
12 B. D. Goddard, A. Nold, N. Savva, P. Yatsyshin and S. Kalliadasis, *J. Phys. Condens. Matter*, 2013, **25**, 035101.
13 A. Nold, *PhD thesis*, Imperial College London, 2016.
14 R. Lhermerout, H. Perrin, E. Rolley, B. Andreotti and K. Davitt, *Nat. Commun.*, 2016, **7**, 12545.
15 N. G. Hadjiconstantinou, *J. Comput. Phys.*, 1999, **265**, 245–

265.
16 J. Zhang, M. K. Borg and J. M. Reese, *Int. J. Heat Mass Transf.*, 2017, **115**, 886–896.
17 J. Koplik, J. R. Banavar and J. F. Willemsen, *Phys. Rev. Lett.*, 1988, **60**, 1282–1285.
18 P. A. Thompson and M. O. Robbins, *Phys. Rev. Lett.*, 1989, **63**, 766–769.
19 Y. Yamaguchi, H. Kusudo, D. Surblys, T. Omori and G. Kikugawa, *J. Chem. Phys.*, 2019, **150**, 044701.
20 D. Seveno, T. D. Blake, S. Goossens and J. De Coninck, *Langmuir*, 2018, **34**, 5160–5161.
21 G. Kikugawa, S. Takagi and Y. Matsumoto, *Comput. Fluids*, 2007, **36**, 69–76.
22 A. P. Willard and D. Chandler, *J. Phys. Chem. B*, 2010, **114**, 1954–1958.
23 E. Chacón and P. Tarazona, *Phys. Rev. Lett.*, 2003, **91**, 1–4.
24 J. Muscatello, E. Chacón, P. Tarazona and F. Bresme, *Phys. Rev. Lett.*, 2017, **119**, 1–5.
25 C. Braga, E. R. Smith, A. Nold, D. N. Sibley and S. Kalliadasis, *J. Chem. Phys.*, 2018, **149**, 044705.
26 L. Bocquet and J.-l. Barrat, *Phys. Rev. E*, 1994, **49**, 3079–3092.
27 S. Chen, H. Wang, T. Qian and P. Sheng, *Phys. Rev. E*, 2015, **92**, 043007.
28 W. Ren and W. E, *Phys. Fluids*, 2007, **19**, 022101.
29 J. Blömer and A. Beylich, *Surf. Sci.*, 1999, **423**, 127–133.
30 P. A. Thompson and S. M. Troian, *Nature*, 1997, **389**, 360–362.
31 S. Nakaoka, Y. Yamaguchi, T. Omori, M. Kagawa, T. Nakajima and H. Fujimura, *Phys. Rev. E*, 2015, **92**, 022402.
32 S. Nakaoka, Y. Yamaguchi, T. Omori and L. Joly, *J. Chem. Phys.*, 2017, **146**, 174702.
33 S. F. Kistler, *Wettability*, Taylor & Francis, 1993, ch. 6, pp. 311–429.
34 R. L. Hoffman, *J. Colloid Interface Sci.*, 1975, **50**, 228–241.
35 L. H. Tanner, *J. Phys. D. Appl. Phys.*, 1979, **12**, 1473–1484.
36 R. G. Cox, *J. Fluid Mech.*, 1986, **168**, 169–194.
37 R. Cox, *J. Fluid Mech.*, 1998, **357**, 249–278.
38 T. Blake and J. Haynes, *J. Colloid Interface Sci.*, 1969, **30**, 421–423.
39 T. Blake and J. De Coninck, *Adv. Colloid Interface Sci.*, 2002, **96**, 21–36.
40 Y. Hizumi, T. Omori, Y. Yamaguchi and T. Kajishima, *Trans. JSME (in Japanese)*, 2015, **81**, 15–00409.
41 S. K. Bhatia and D. Nicholson, *Langmuir*, 2013, **29**, 14519–14526.
42 K. Falk, F. Sedlmeier, L. Joly, R. R. Netz and L. Bocquet, *Langmuir*, 2012, **28**, 14261–14272.